Matter, Volume *4*

Supplemental information

Discovering giant magnetoelasticity in soft matter for electronic textiles

Guorui Chen, Xun Zhao, Sahar Andalib, Jing Xu, Yihao Zhou, Trinny Tat, Ke Lin, and Jun Chen

Supplemental Information

Discovering giant magnetoelasticity in soft matter for electronic textiles

Guorui Chen[1,2], Xun Zhao[1,2], Sahar Andalib[1], Jing Xu[1], Yihao Zhou[1], Trinny Tat[1], Ke Lin[1], Jun Chen[1]*

[1]Department of Bioengineering, University of California, Los Angeles, Los Angeles, CA 90095, USA

[2]These authors contributed equally to this work.

*Correspondence to: jun.chen@ucla.edu (J.C.)

Contents

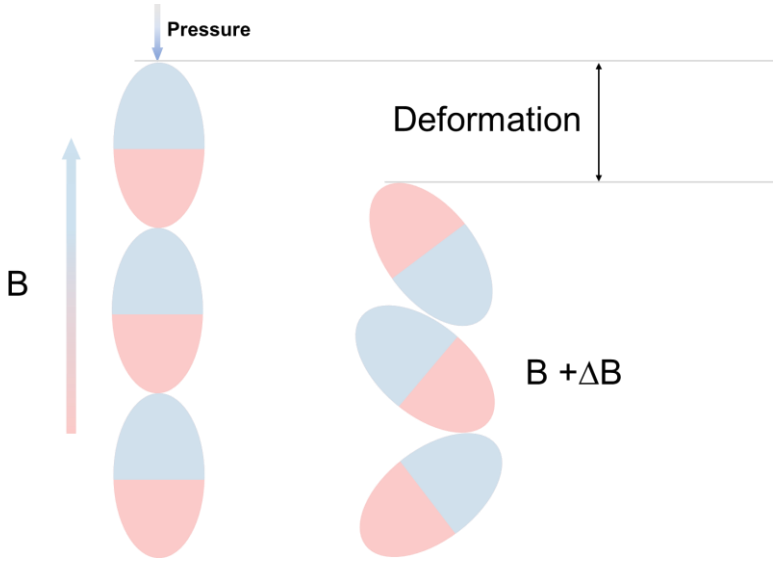

Figure S1. Schematic illustration of the magnetoelasticity. Magnetoelastic effect is defined as the change of any magnetic property in certain materials under mechanical deformation.[1]

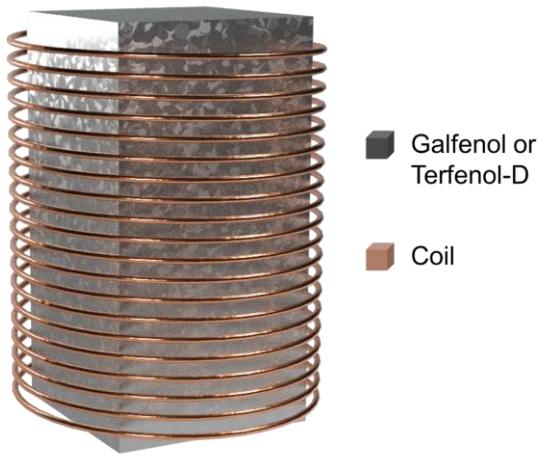

Figure S2. Conventional magnetoelasticity system based on the rigid Galfenol or Terfenol-D for mechanical-to-electrical conversion. Rigid magnetoelastic materials such as the Galfenol or Terfenol-D can be deformed by external pressure and generate the magnetization variation.[2,3] The corresponding magnetic flux density change will induce an electromotive force in the rigid coils based on Faraday's law of induction.

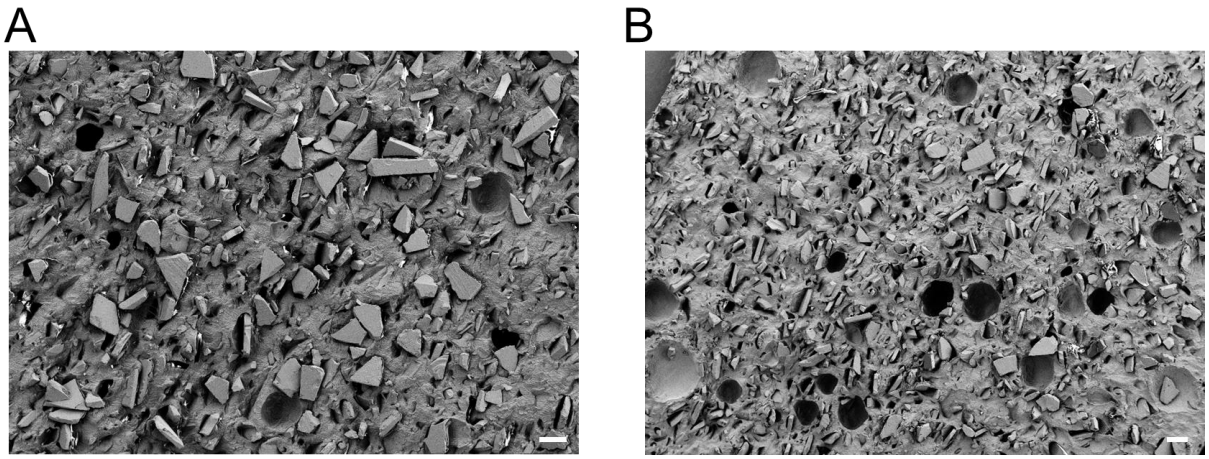

Figure S3. SEM pictures of the soft magnetoelastic film. (A) and (B) SEM pictures of the soft magnetoelastic film. These micromagnets are evenly distributed in the porous polymer matrix. Scale bars, 100 μm.

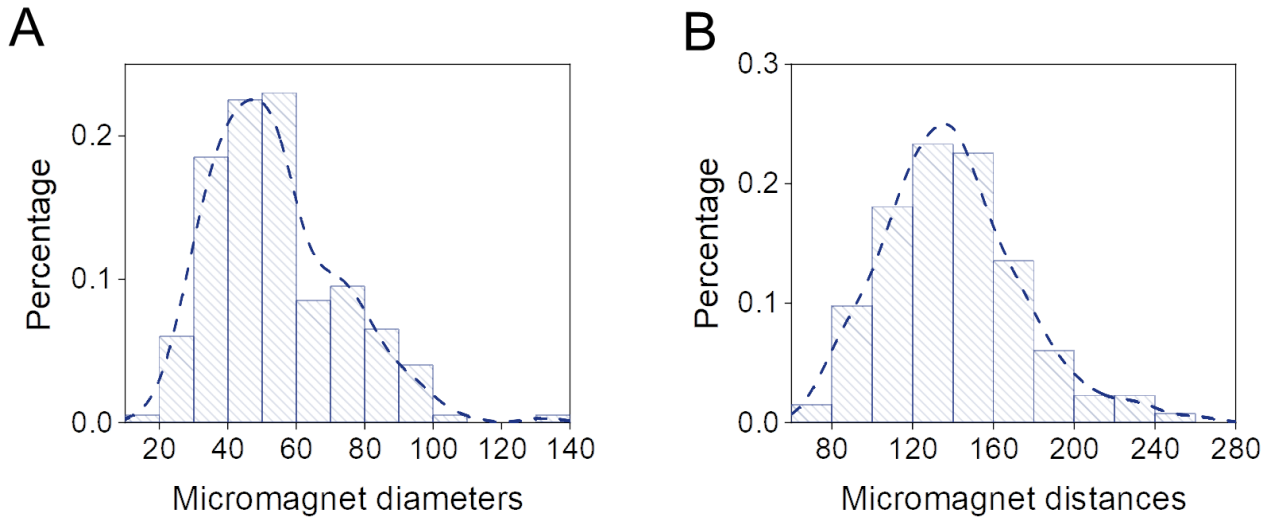

Figure S4. Size and inter-particle distribution of the micromagnets in the polymer matrix.

(A) These micromagnets have a mean diameter of 53.7 μm with a standard deviation of 18.8 μm.

(B) These micromagnets have a mean interparticle distance of 139.6 μm with a standard deviation of 34.0 μm.

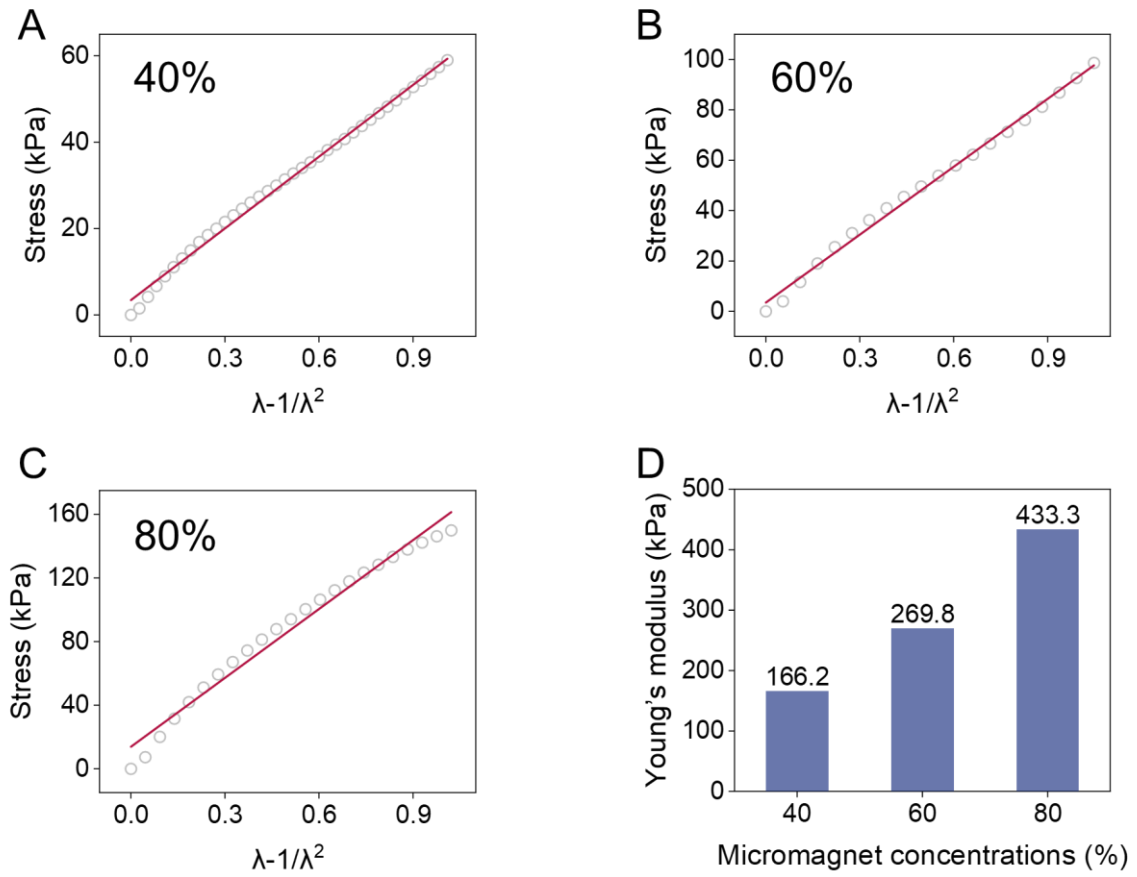

Figure S5. Calculating the Young's modulus of the soft magnetoelastic film with different micromagnet concentrations by using Neo-Hookean model.

(A) Calculating the Young's modulus of the soft magnetoelastic film with 40 wt% micromagnet concentrations.

(B) Calculating the Young's modulus of the soft magnetoelastic film with 60 wt% micromagnet concentrations.

(C) Calculating the Young's modulus of the soft magnetoelastic film with 80 wt% micromagnet concentrations.

(D) Young's modulus of the soft magnetoelastic film with different micromagnet concentrations.

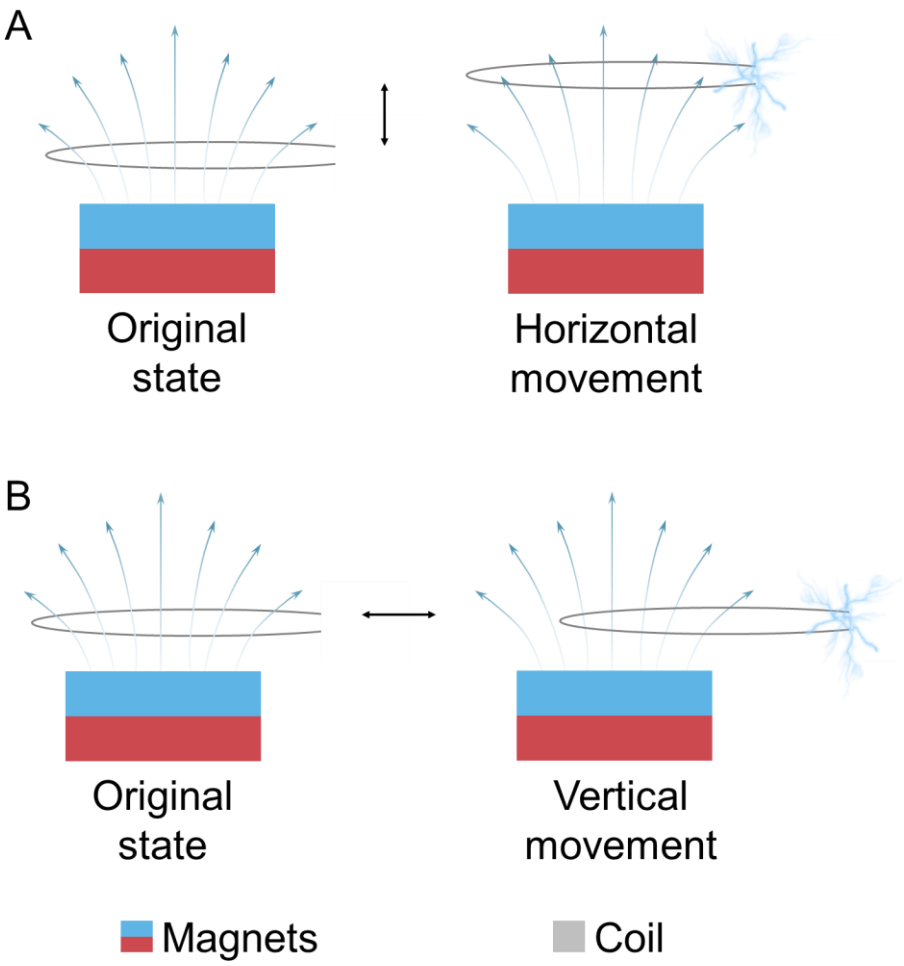

Figure S6. Working mechanisms of the wearable electromagnetic generators. (A) and (B) Conventional electromagnetic generators require the magnets moving relative to coils, such as the horizontal movement (A) and the vertical movement (B), thus generating a motional electromotive force based on Faraday's law of induction.

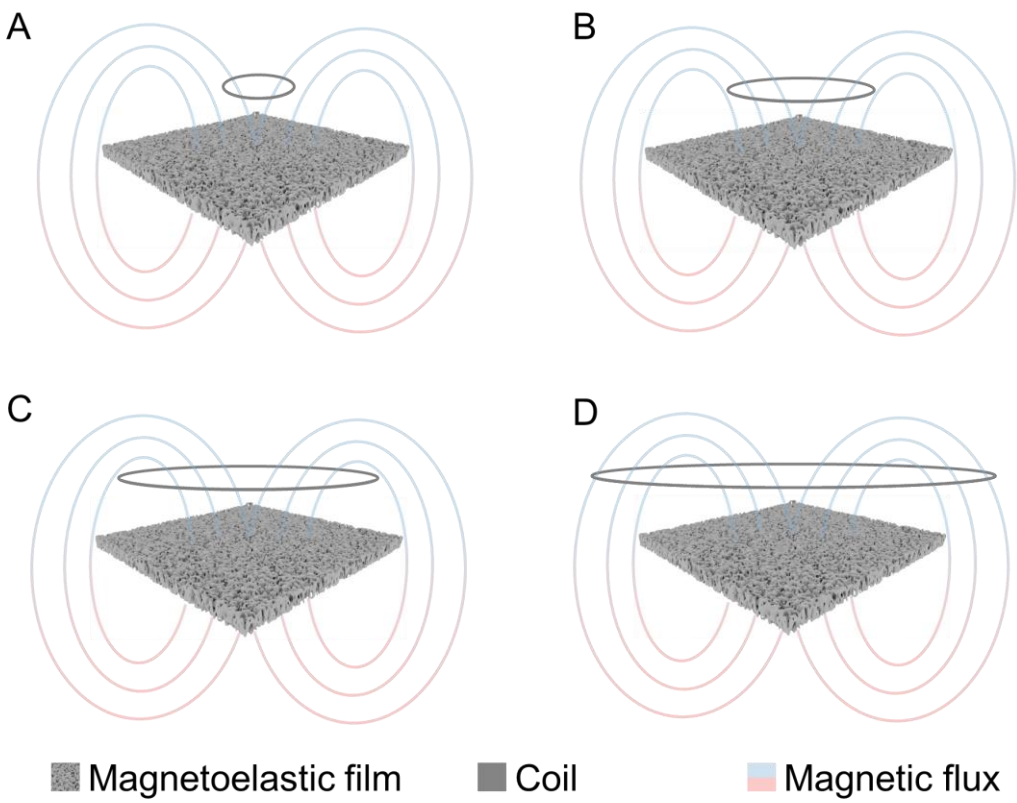

Figure S7. Dependence of the magnetic field variation on the area ratio of the coil and the soft magnetoelastic film.

(A) and (B) A smaller coil ($S_{coil}/S_{film} < 1$) cannot collect all magnetic flux variation of the compressed the soft magnetoelastic film.

(C) Approximately same size of the coil and the soft magnetoelastic film is the optimized ratio to take use of the magnetic field variation.

(D) A large coil ($S_{coil}/S_{film} > 1$) consists of adverse magnetic flux canceling each other out.

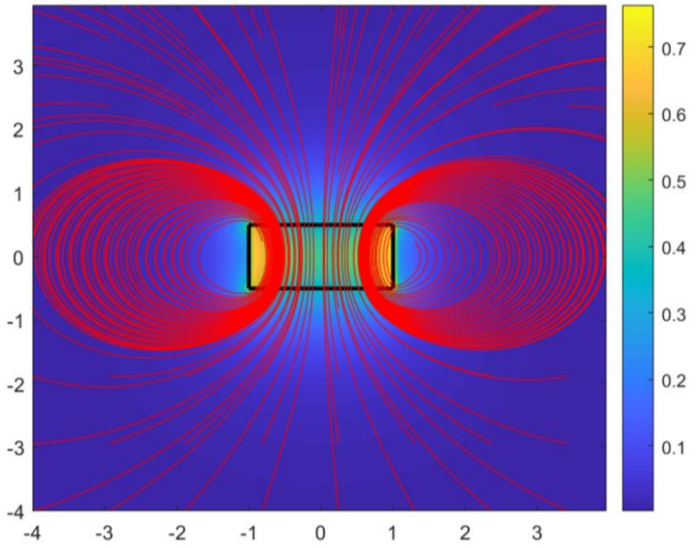

Figure S8. Magnetic fields distribution of the magnets. MATLAB stimulation demonstrates that the density of the magnetic flux decreases with the distance to the magnets. Thus, textile coil closely attached to the soft magnetoelastic film could well take use of the magnetic flux variation and generate the maximum electric outputs.

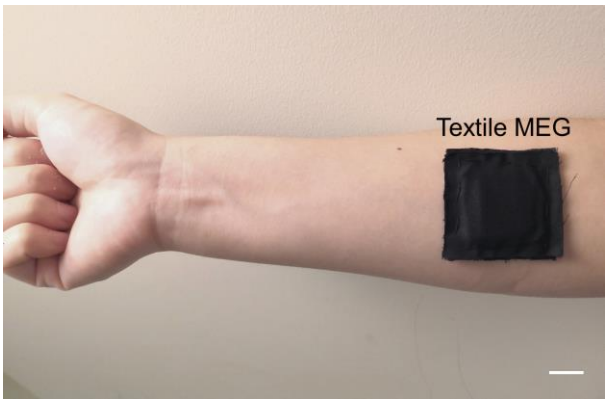

Figure S9. Photograph of the textile MEG conformably attached to the human skin. This textile MEG can be conformably attached to the human skin owing to its high flexibility. Scale bar, 1cm.

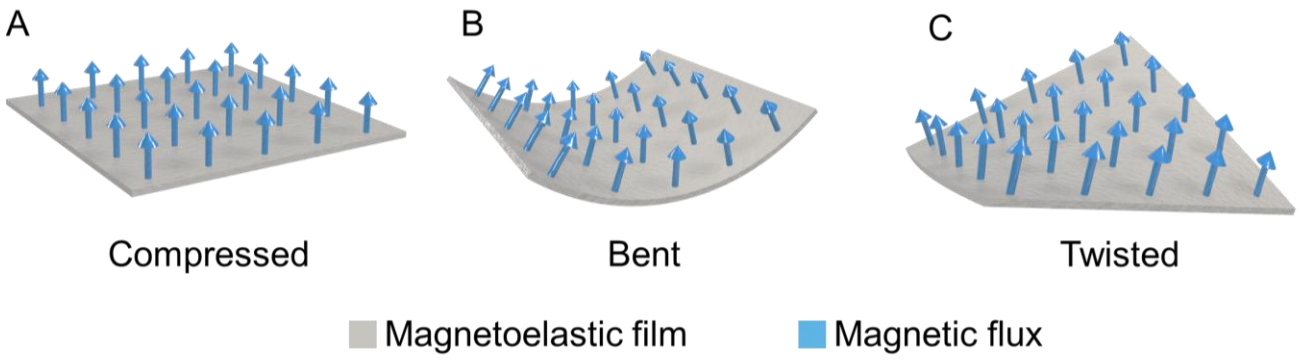

Figure S10. The soft magnetoelastic films under the compressed, bent, and twisted state.

(A) Vertically applied pressure on the compressed soft magnetoelastic film could strongly decrease the magnetic flux density.

(B) and (C) The bent (B) and twisted (C) soft magnetoelastic film would partially cancel the magnetic field variation, because some flux demonstrates the opposite direction.

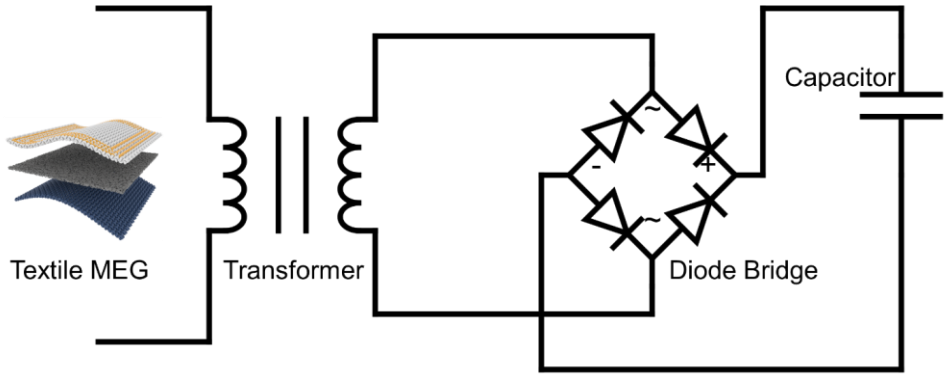

Figure S11. Circuit diagram of the booster and rectifier. The equivalent circuit to boost the voltage and rectify the alternative electric output of the textile MEG into the direct output.

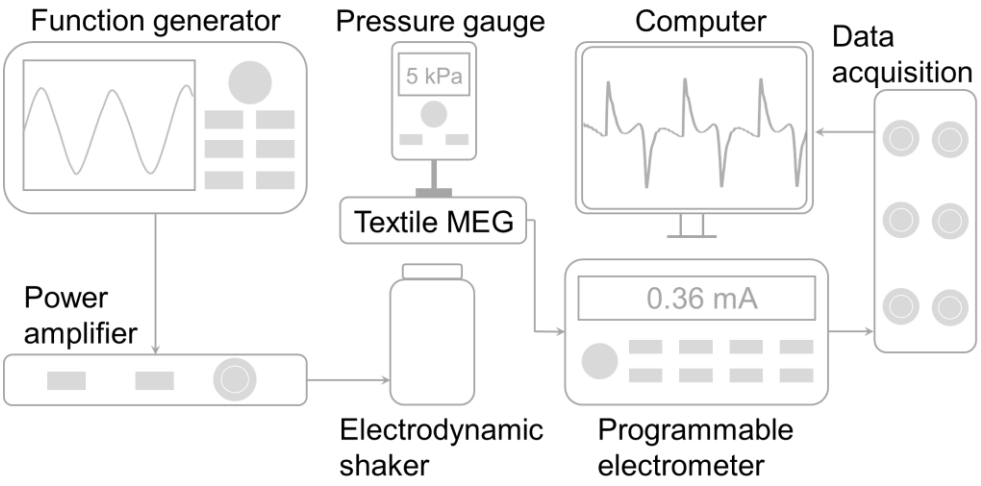

Figure S12. Schematic illustration of the experimental setup for sensing performance characterization. A testing system containing a function generator, power amplifier, electrodynamic shaker, pressure gauge, programmable electrometer, and computer.

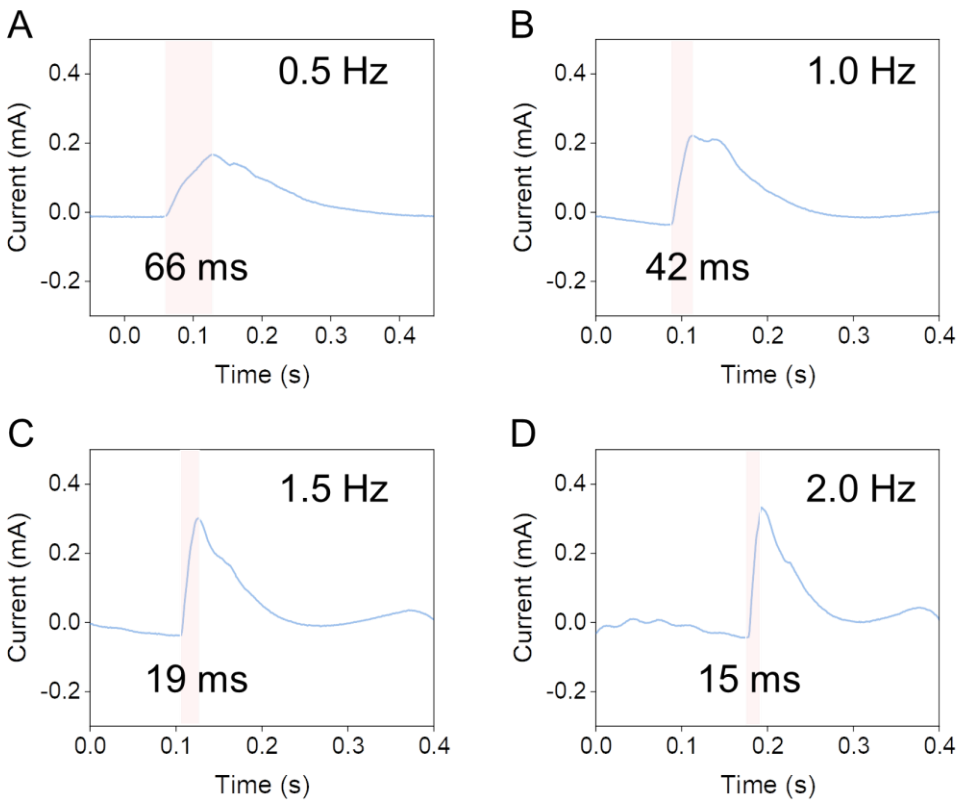

Figure S13. Response time of the textile MEG. External pressure excitation with the input frequency of (A) 0.5 Hz, (B) 1.0 Hz, (C) 1.5 Hz, (D) 2.0 Hz were applied on the textile MEG. The response time of the textile MEG is 66 ms, 42 ms, 19 ms, and 15 ms, respectively.

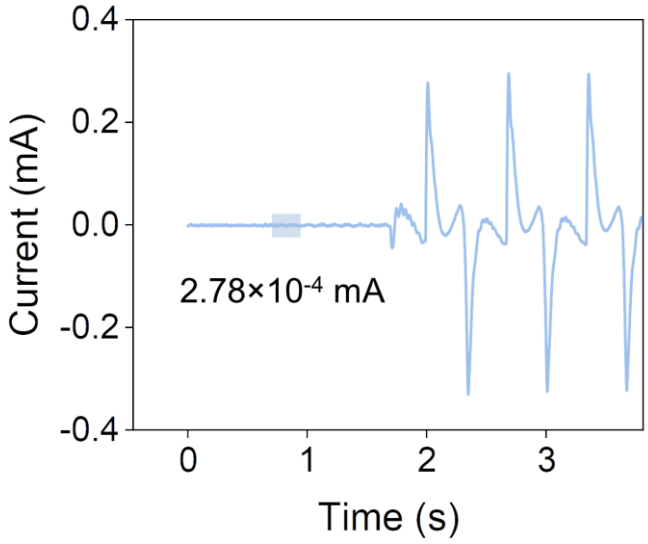

Figure S14. Signal-noise-ratio (SNR) measurement of the textile MEG. The SNR of the textile MEGs is calculated by $20 \times \lg(I_{signal}/I_{noise})$. The average noise of our measurement system is 2.78×10^{-4} mA.

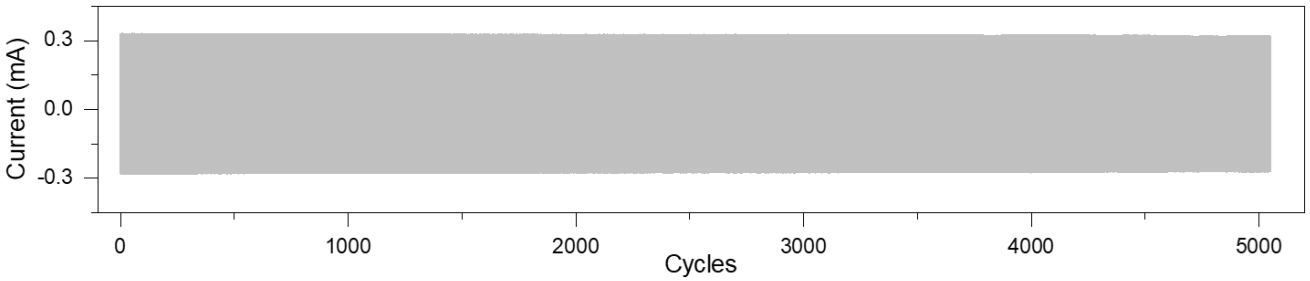

Figure S15. The stability test of the textile MEG. An amplitude-fixed pressure with a frequency of 2 Hz was applied to the textile MEG for 5,000 loading-unloading cycles.

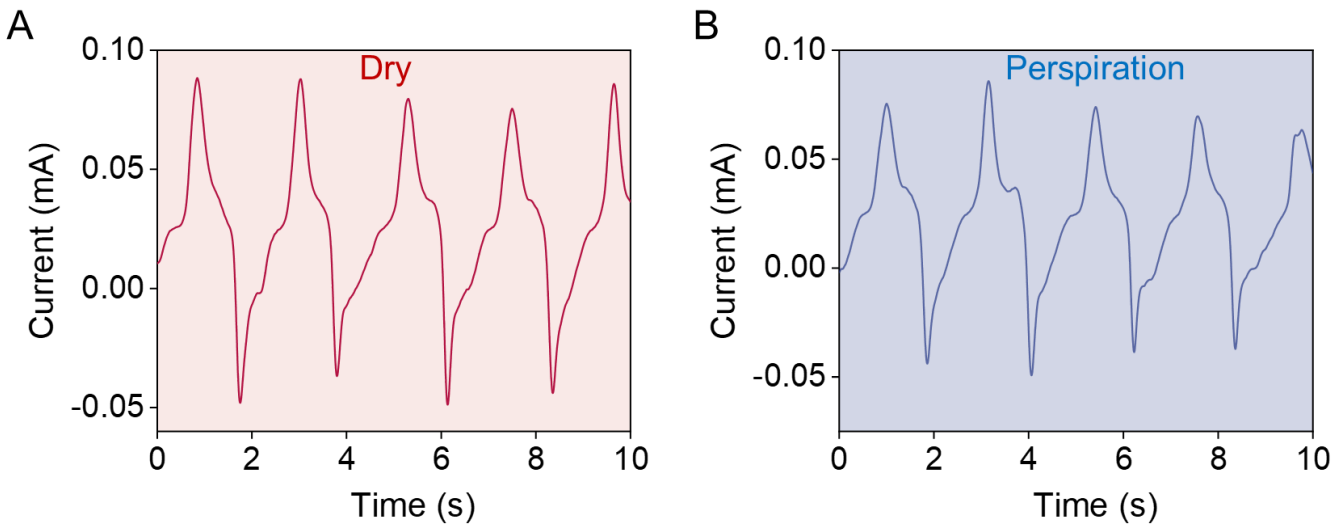

Figure S16. The sweatproof ability test of the textile MEG.

(A) and (B) Comparison of the respiratory signal waveforms obtained from the textile MEG under dry situation (A) and with artificial perspiration (B).

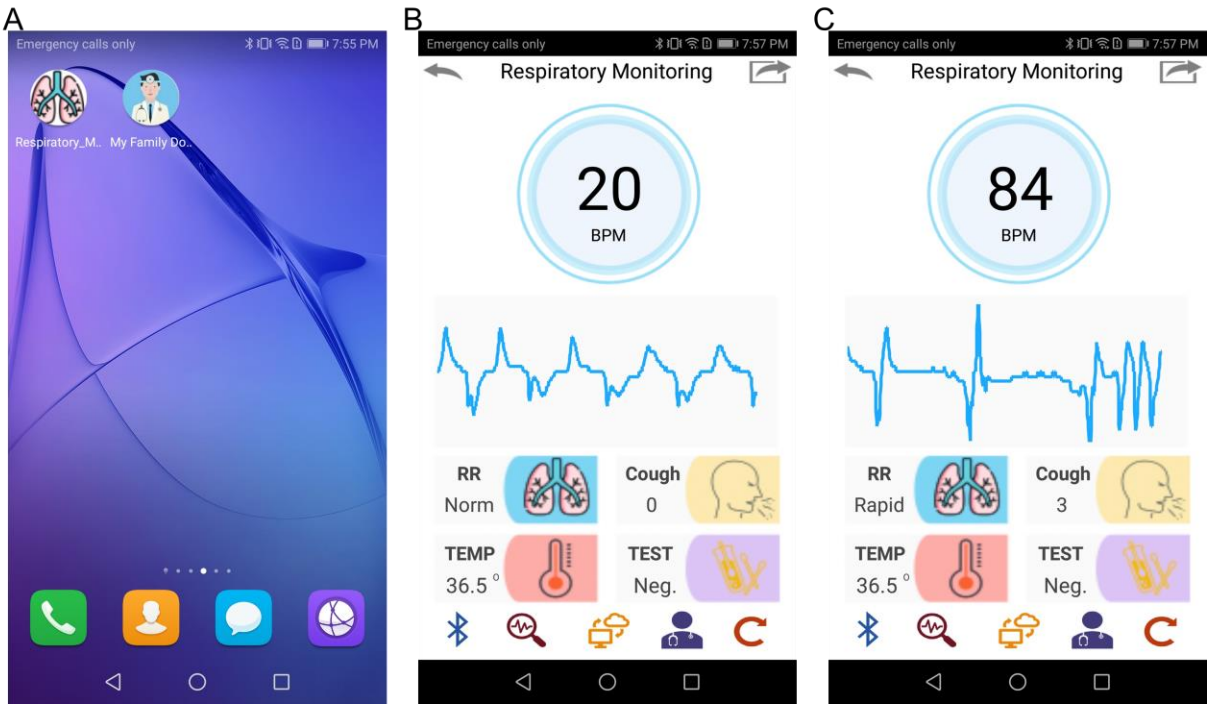

Figure S17. Customized cellphone APP for respiratory monitoring data display.

(A) APP's icon on a cellphone desktop.

(B) and (C) APP interfaces showing the breaths per minute (BPM), respiratory rate (RR), cough, temperature, and test results of a young adult user under different status.

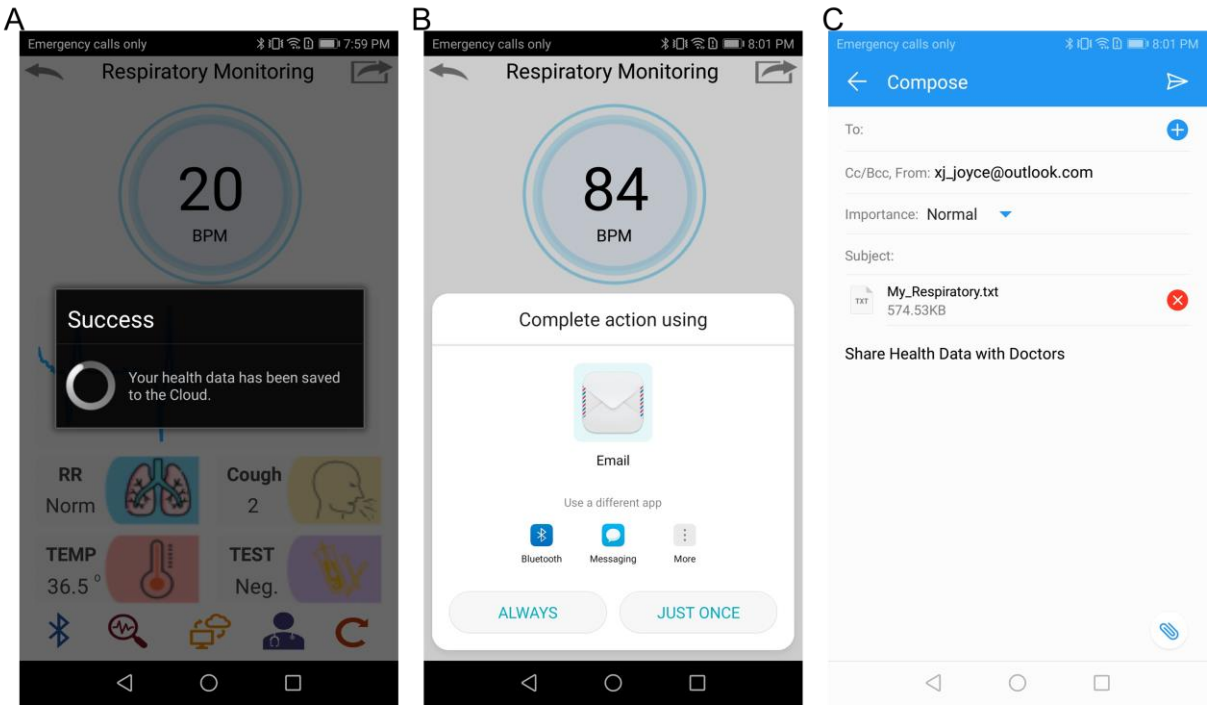

Figure S18. Customized cellphone APP for respiratory monitoring data storage and sharing.

(A) Customized cellphone APP can save the respiratory monitoring data to the cloud for further analysis.

(B) Customized cellphone APP can share the respiratory monitoring data through email, Bluetooth, or messaging.

(C) APP interface showing the personalized respiratory monitoring data sent to a physician through email.

Table S1. Performance comparison of our work with conventional magnetoelasticity systems.[6]

Systems	Magnetomechanical coupling factor (T/Pa)	Young's modulus (kPa)	Applied pressure range (kPa)	External magnetic field
Terfenol-D	1.36×10^{-8} [2]	1.2×10^{8} [4]	Megapascal [2]	Required [3]
Galfenol	3.85×10^{-8} [3]	7.6×10^{7} [5]	Megapascal [4]	Required [3]
Our work	6.77×10^{-8}	433.3	Kilopascal	Not Required

Table S2. Average accuracy for cross validation.

Classifier	Features	Feature Type	Number of features	Average Accuracy (%)
Decision tree	minimal	all	9	73.61
	minimal	selected/filtered	5	72.79
	efficient	all	781	80.61
	efficient	selected/filtered	248	82.12
Random forest	minimal	all	9	79.45
	minimal	selected/filtered	5	78.62
	efficient	all	781	90.89
	efficient	selected/filtered	248	89.49

Table S3. Test results for decision tree classifier.

Feature (Type)	Average Accuracy (%)	AUC	Mode	Precision	Recall	F-score
minimal (all)			normal	0.71	0.65	0.68
minimal (all)	61.32	0.68	rapid	0.62	0.32	0.42
minimal (all)			cough	0.53	0.77	0.63
minimal (filtered)			normal	0.66	0.67	0.67
minimal (filtered)	58.49	0.66	rapid	0.53	0.32	0.4
minimal (filtered)			cough	0.52	0.66	0.58
efficient (all)			normal	0.8	0.72	0.76
efficient (all)	66.98	0.74	rapid	0.54	0.56	0.55
efficient (all)			cough	0.62	0.69	0.65
efficient (filtered)			normal	0.5	0.11	0.18
efficient (filtered)	34.91	0.50	rapid	0	0	0
efficient (filtered)			cough	0.33	0.91	0.49

Table S4. Test results for random forest classifier.

Feature (Type)	Average Accuracy (%)	AUC	Mode	Precision	Recall	F-score
minimal (all)			normal	0.67	0.74	0.7
minimal (all)	63.21	0.78	rapid	0.32	0.38	0.47
minimal (all)			cough	0.66	0.71	0.68
minimal (filtered)			normal	0.64	0.74	0.69
minimal (filtered)	61.32	0.74	rapid	0.54	0.28	0.37
minimal (filtered)			cough	0.6	0.69	0.64
efficient (all)			normal	0.79	0.89	0.84
efficient (all)	73.58	0.82	rapid	0.58	0.6	0.59
efficient (all)			cough	0.79	0.63	0.7
efficient (filtered)			normal	0	0	0
efficient (filtered)	33.02	0.640	rapid	0	0	0
efficient (filtered)			cough	0.33	1	0.5

Supplemental References

1. Deng, Z., and Dapino, M.J. (2018). Review of magnetostrictive materials for structural vibration control. Smart Mater. Struct. *27*, 113001.
2. Liu, J., Jiang, C., and Xu, H. (2012). Giant magnetostrictive materials. Sci. China Technol. Sci. *55*, 1319-1326.
3. Deng, Z. (2015). Nonlinear modeling and characterization of the villari effect and model-guided development of magnetostrictive energy harvesters and dampers. (The Ohio State University).
4. Su, Q., Morillo, J., Wen, Y., and Wuttig, M. (1996). Young's modulus of amorphous terfenol-d thin films. J. Appl. Phys. *80*, 3604-3606.
5. Datta, S., Atulasimha, J., Mudivarthi, C., and Flatau, A.B. (2010). Stress and magnetic field-dependent young's modulus in single crystal iron–gallium alloys. J. Magn. Magn. Mater. *322*, 2135-2144.
6. Zhou, Y., Zhao, X., Xu, J., Fang, Y., Chen, G., Song, Y., Li, S., and Chen, J. (2021). Giant magnetoelastic effect in soft systems for bioelectronics. Nat. Mater. DOI:10.1038/s41563-021-01093-1

Video S1. Micro-computed tomography of the soft matter with micromagnets.
Supplemental Video 1 is available in the online version of the paper.

Video S2. Textile MEGs for ultra-low-pressure sensing.
Supplemental Video 2 is available in the online version of the paper.

Video S3. Customized cellphone APP for respiratory monitoring.
Supplemental Video 3 is available in the online version of the paper.